Biosensors and Bioelectronics 262 (2024) 116544



Contents lists available at ScienceDirect

Biosensors and Bioelectronics

journal homepage: www.elsevier.com/locate/bios



Laser-assembled conductive 3D nanozyme film-based nitrocellulose sensor for real-time detection of H_2O_2 released from cancer cells

Qurat U.A. Bukhari [a,b,1], Flavio Della Pelle [b,1], Ruslan Alvarez-Diduk [a,*], Annalisa Scroccarello [b], Carme Nogués [c], Oriol Careta [c], Dario Compagnone [b,**], Arben Merkoci [a,d,***]

[a] Nanobioelectronics & Biosensors Group, Catalan Institute of Nanoscience and Nanotechnology (ICN2), CSIC and BIST, Campus UAB, Bellaterra, Barcelona, Spain
[b] Department of Bioscience and Technology for Food, Agriculture and Environment, University of Teramo, Campus "Aurelio Saliceti" Via R. Balzarini 1, 64100, Teramo, Italy
[c] Departament de Biologia Cellular, Fisiologia i Immunologia, Facultat de Biociencies, Universitat Autonoma de Barcelona (UAB), 08193 Bellaterra, Barcelona, Spain
[d] ICREA Institució Catalana de Recerca i Estudis Avançats, Passeig de Lluís Companys, 23, 08010, Barcelona, Spain

ARTICLE INFO

Keywords:
Biosensors
Paper-based sensors
Nanozymes
IR laser
Cells
Nanomaterial film

ABSTRACT

In this work, a nanostructured conductive film possessing nanozyme features was straightforwardly produced via laser-assembling and integrated into complete nitrocellulose sensors; the cellulosic substrate allows to host live cells, while the nanostructured film nanozyme activity ensures the enzyme-free real-time detection of hydrogen peroxide (H_2O_2) released by the sames. In detail, a highly exfoliated reduced graphene oxide 3D film decorated with naked platinum nanocubes was produced using a CO_2-laser plotter via the simultaneous reduction and patterning of graphene oxide and platinum cations; the nanostructured film was integrated into a nitrocellulose substrate and the complete sensor was manufactured using an affordable semi-automatic printing approach. The linear range for the direct H_2O_2 determination was 0.5–80 μM ($R^2 = 0.9943$), with a limit of detection of 0.2 μM. Live cell measurements were achieved by placing the sensor in the culture medium, ensuring their adhesion on the sensors' surface; two cell lines were used as non-tumorigenic (Vero cells) and tumorigenic (SKBR3 cells) models, respectively. Real-time detection of H_2O_2 released by cells upon stimulation with phorbol ester was carried out; the nitrocellulose sensor returned on-site and real-time quantitative information on the H_2O_2 released proving useful sensitivity and selectivity, allowing to distinguish tumorigenic cells. The proposed strategy allows low-cost in-series semi-automatic production of paper-based point-of-care devices using simple benchtop instrumentation, paving the way for the easy and affordable monitoring of the cytopathology state of cancer cells.

1. Introduction

Diagnostic approaches to detect and monitor markers of severe degenerative diseases such as cancer, neurodegenerative disorders, and arteriosclerosis, are strongly needed to advance knowledge, use appropriate therapies and follow their progress. Nowadays, the evaluation of physical symptoms and invasive techniques are used in this respect (Morais et al., 2022; Rojas et al., 2022; Young, 2009), while in the near future therapies are expected to be personalized based on genetic and biochemical patterns; the search for biomarkers able to return information is, then, needed, together with easy and portable analytical devices to follow their evolution (Young, 2009). Among biomarkers, hydrogen peroxide (H_2O_2), naturally occurring in trace in healthy conditions (Jiao et al., 2020; Lennicke et al., 2015; Meier et al., 2019; Trujillo et al., 2021), is involved in molecular signaling and immunity, and can be considered a metabolic by-product (Lennicke et al., 2015; Meier et al., 2019); because of its relative stability, H_2O_2 is the most representative physiological reactive oxygen species (ROS) (Rojas et al.,

* Corresponding author.
** Corresponding author.
*** Corresponding author. Nanobioelectronics & Biosensors Group, Catalan Institute of Nanoscience and Nanotechnology (ICN2), CSIC and BIST, Campus UAB, Bellaterra, Barcelona, Spain.
E-mail addresses: ruslan.alvarez@icn2.cat (R. Alvarez-Diduk), dcompagnone@unite.it (D. Compagnone), arben.merkoci@icn2.cat (A. Merkoci).
[1] Q.U.A. Bukhari, and F. Della Pelle contributed equally to this paper.

https://doi.org/10.1016/j.bios.2024.116544
Received 17 April 2024; Received in revised form 25 June 2024; Accepted 27 June 2024
Available online 29 June 2024
0956-5663/© 2024 The Authors. Published by Elsevier B.V. This is an open access article under the CC BY license (http://creativecommons.org/licenses/by/4.0/).

2022). Overproduction and dysregulation of H_2O_2 indicate oxidative stress conditions and/or oxidative homeostasis perturbation, that are prone to activate cascades of disruptive reactions towards proteins, lipids, and DNA in the brain and/or other tissues, promoting negative effects in degenerative disease (Dong et al., 2018; Lee et al., 2020; Morais et al., 2022; Schumacker, 2015); H_2O_2 can be considered a marker for pathological states. Among others, cancer cells, because of the enhanced oxidative metabolic activity, overproduce ROS; thus the H_2O_2 release, under chemical stimuli, can return real-time information related to the cancer cells' pathological state (Lee et al., 2020; Lennicke et al., 2015).

For the above reasons, several strategies have been developed for the detection of H_2O_2, and considerable efforts have been made to apply these methods directly in live cells. Highly sensitive methods based on spectrophotometry, fluorescence, and chemiluminescence have been proposed. However, these techniques do not allow direct measurement of H_2O_2 and make real-time detection very difficult. On the other hand, the recent advances in electrochemical biosensing have made it possible to directly monitor H_2O_2 released by cancer cells (Dong et al., 2018; Rojas et al., 2020; Zhao et al., 2021). Nonetheless, most of the electrodes proposed use commercial transducers (glassy carbon electrodes, screen-printed electrodes, etc.) characterized by limited customizability and biocompatibility, where the ability to detect hydrogen peroxide is conferred through the integration of mediators or enzymes added in additional steps, which further complicate the sensor fabrication and use. In this context, the enormous progress associated with the discovery and development of new nanomaterials with specific properties has opened the door to the development of sensors and electrochemical devices capable of directly monitoring H_2O_2. In this direction, increasing efforts are currently being made to integrate films of functional nanomaterials into all-in-one devices, that can directly host live cells and allow in situ and real-time measurements (Morais et al., 2022; Rojas et al., 2022); although many efforts have been made, complex and expensive machinery and clean rooms are often required for their manufacture.

Carbon-based nanomaterials (C-NMs) decorated with metal nanostructures have become the preferred sensing surfaces for the detection of H_2O_2, with properties comparable to enzyme-like activity; for this reason, they are also referred to as nanozymes (Trujillo et al., 2021; Zhao et al., 2021). Among C-NMs, graphene (G) and G-based nanocomposites (G-NCs) have attracted great interest due to their large surface area, superior electronic and electron transfer capability, and compatibility with biological molecules and live cells (Coroş et al., 2020). G-NCs are conventionally realized using different G precursors (i.e., graphene oxide/GO, graphite, graphite oxide) (Inagaki and Kang, 2014; X. Liu et al., 2021); among them, GO allows to easily host and stabilize metal-nanostructures (Dideikin and Vul', 2019). The electronic/electrochemical properties of GO can be easily enhanced by chemical reduction to reduced graphene oxide (rGO); this can be achieved by different strategies leading to different nanoarchitectures (Gurunathan et al., 2019). Due to its high versatility, rGO has been used to develop a plethora of (bio)sensing platforms for H_2O_2 determination (Coroş et al., 2020; Dideikin and Vul', 2019; Zhang et al., 2019; Zhu et al., 2019). Jiao et al. modified a glassy carbon electrode (GCE) with chemically synthesized gold-silver-platinum nanoalloy on a polymer-capped rGO nanostructure for the detection of H_2O_2 release from different cancer cell lines (i.e., SKOV3 cells, human ovarian cancer; MCF-7, breast cancer, A431, epidermoid carcinoma) (Jiao et al., 2020); the formation of the nanocomposite required more than 24 h and the GCE was modified by dip-coating. Dong et al. used a gold-platinum-palladium nanoalloy/rGO-modified GCE to monitor H_2O_2 in live cancer cells (Dong et al., 2018); in this case, the nanostructure was chemically prepared using a process that requires more than 4 h. In both approaches, the measurement is performed by immersing the electrode in buffer in the presence of washed and purified cells. It is noteworthy that, platinum-nanoparticles (PtNPs) integrated into conductive nanomaterials or electrodic surfaces are the most widely used metal-based structures for H_2O_2 detection, due to their well-known peroxidase-like activity (Jiao et al., 2020; Lee et al., 2020; Liu et al., 2014; Proa-Coronado et al., 2018). However, their use to fabricate lab-made sensors with accessible techniques on flexible substrates is still poorly explored, especially for live cell-based biosensors; moreover, the need for commercial transducers and complex nanocomposite 'synthesis' limits their use and integration within everyone's reach devices.

The laser photothermal (LPT) approach is one of the most advanced, affordable, and attractive in this decade for the fabrication of graphene nanostructures and NCs. LPT allows to easily obtain graphene/rGO films (Giacomelli et al., 2020) starting from polymide/GO, with tailored patterns and submicrometric accuracy with a reagent and solvent-free approach (Li, 2020). Noteworthy, rGO produced via LPT approaches results easily transferable on different flexible substrates preserving their features (Zhao et al., 2023), offering infinitive and customizable opportunities for electrochemical device developments. LPT-based strategies can allow further decoration with various additional nanomaterials, offering tremendous potential for the patterning, structuring, and electrochemical tuning of nanostructures. In particular, different works report the ability of LPT to generate NCs composed of laser-induced graphene integrating metal-nanoparticles (Rodrigues et al., 2019; Scroccarello et al., 2023; You et al., 2020). Due to its versatility, LPT can be easly combined with affordable electrochemical device fabrication (i.e., 3D printing, inkjet printing, xurography, etc.) (Li, 2020; Rocha et al., 2021).

In this context, cellulose-based substrates have recently been used in (bio)sensor development due to their unique and sustainable physicochemical properties and low-cost, making (bio)sensor fabrication scalable and affordable, and often bio-compatible (Liu et al., 2014; M. M. Liu et al., 2021). To the best of our knowledge, only one article reports the use of cellulose for the real-time determination of H_2O_2 released by cancer cells. The electrode was fabricated using carbon-based ink; a paper-based disk was decorated with PtNPs by drop-casting, the PtNPs were subsequently grown in-situ using an external reducing agent, and housed onto the working electrode. Cancer cells were immobilized into the paper disk using aptamers, and anticancer drugs were screened by evaluating the H_2O_2 produced by the cells (Liu et al., 2014). This work demonstrates the ability of cellulose to host both cells and PtNPs as a sensing element, despite the cumbersome sensor fabrication process (Liu et al., 2014; M. M. Liu et al., 2021). In this framework, despite the infinite possibilities offered by the fabrication of graphene structures using LPT strategies, the straightforward development of nanostructured films with nanozyme functions to fabricate paper-based sensors able to host and measure live cells is not reported.

Herein, lab-made nitrocellulose sensors were fabricated using laser-assembled conductive 3D film with nanozyme activity. The laser treatment drives the immediate and straightforward formation of a nanostructured 3D framework of rGO decorated with Pt-nanocubes with marked electrocatalytic activity toward H_2O_2. The PtNPs-rGO film was integrated into nitrocellulose (NTC) and the complete sensor (NTC/PtNPs-rGO) was manufactured using a stencil-printing low-cost approach. The sensor was fully physicochemically characterized, and the electrocatalytic and electroanalytical features studied. The sensor's ability to host live cells was proved, and it was used for the in situ and real-time detection of H_2O_2 released from non-tumorigenic and tumorigenic live cells under chemical stimulation. This work proves how lasser-assembled nanomaterials can possess useful nanozyme features, and how the resulting nanofilms are integrable in modern complete paper-based devices able to host and measure live cells.

2. Material and methods

2.1. Chemicals and materials

A detailed description is reported in *section SM.2.1*.

2.2. Substrates and apparatus

A detailed description is reported in *section SM.2.2*.

2.3. PtNPs-rGO nanostructured film laser-assembling and NTC/sensors manufacturing

Fig. S1 sketches the fabrication of the NTC sensors integrating the PtNPs-rGO laser-assembled film. 10 mg mL^{-1} GO were diluted in 5 mL of a 30 mM Pt(II) solution to reach the final concentration of 1 mg mL^{-1}; the film components amount was selected according to Scroccarello et al. (2023). The Pt(II)/GO dispersion was stirred for 5 min and then vacuum filtered using the PVDF membrane (**a**). The film was left to dry at room temperature for 20 min and then treated with the CO_2-laser. The engraving mode was used as follows: z-distance 7.4 cm from the focusing lens, laser power/LP 2.10 W, laser speed/LP 1.50 m s^{-1}; for each filter eight WE and CE were obtained. Key-lock-like working electrodes were laser-scribed using Corel Draw software to obtain an exposed circular geometrical area of Ø = 3 mm, while counter electrodes (lateral section 1 mm) were scribed with a hook shape to surround the WE (**b**). To facilitate alignment with contacts and the film transfer, WE and CE pairs were cut in small rectangles (10 mm × 7 mm), using the CO_2-laser at higher power (7.4 cm focusing lens; LP 7.60 W; LS 0.75 m s^{-1}) (**c**).

The sensors were built onto nitrocellulose (NTC) rectangles (25 mm × 10 mm) obtained from an NTC reel. Conductive silver ink was used to print the electrical contacts and the reference electrode (RE) by using a complementary stencil mask designed and patterned using a cutter-plotter. The stencil mask was fabricated according to the complementary desired pattern and then attached to NTC reel, then the silver conductive ink was spread by squeegee. The stencil mask was removed and then the silver ink was cured at 100 °C for 10 min (**d**). The PtNPs-rGO WE and CE were transferred onto the NTC aligning the complementary silver contacts, applying a pressure of 3.0 ± 0.1 t for 3 min (**e**). Eventually, the contacts were insulated by dielectric paste and cured at 100 °C for 15 min (**f**). The complete sensor is ready to use and does not need pre-treatment/activation; for the SKBR-3 cell analysis, the sensor was placed in the bottom of specially modified 35 mm Petri dishes (**g**) and sterilized under UV light for 5 min.

2.4. Morpho-chemical characterization

A detailed description is reported in *section SM.2.4*.

2.5. Cells electrochemical measurement

SKBR-3 cells, a tumorigenic human mammary epithelial cell line (ATCC, USA), were cultured in McCoy's 5 A modified medium (Gibco, UK) supplemented with 10% fetal bovine serum (FBS; Gibco) in a 37 °C humidified incubator set to 5% CO_2 (standard culture conditions). As a non-tumorigenic, Vero cells (ATCC), a cell line derived from the kidney of an African green monkey, were cultured in Minimum Essential Media (MEM; Gibco) supplemented with 10% FBS (Gibco) under standard conditions.

The potential cytotoxic effect of the NTC/PtNPs-rGO sensor was evaluated with $1x10^6$ and $2x10^6$ SKBR3 and Vero cells seeded in modified 35 mm plates with inserted electrodes. After 24 h, in standard conditions, cell viability was evaluated using the Live/Dead viability/Cytotoxicity kit for mammalian cells (Invitrogen), according to the manufacturer's protocol. Images from different regions of the cells grown on modified (sensor) or standard plates (control), were captured using an Olympus IX71 inverted microscope equipped with epifluorescence. Experiments were performed in triplicate.

To validate the NTC/PtNPs-rGO sensor for H_2O_2 detection, three different amounts ($0.5x10^5$, $1x10^5$ and $2x10^5$) of SKBR-3 and Vero cells were seeded in the same modified 35 mm plates with inserted electrodes for 24 h in standard conditions. The incubation solution was removed and 30 μL of phosphate buffer (PB) was placed on the sensor measuring zone, the potential was set at + 0.4 V and the current was left to stabilize. After the signal stabilization, the cells were stressed by adding Phorbol 12-myristate 13-acetate (PMA) directly into the PB solution; the change in current was used as signal. The cells were stimulated by adding the same volume of the stressor and varying the concentration of the PMA working solution. Experiments were performed in triplicate.

Fig. S6a

3. Results and discussion

This work aims to propose an innovative approach for the development of paper-based electrochemical sensors that can be used for real-time detection of hydrogen peroxide (H_2O_2) released by live cancer cells. In particular, a CO_2 laser-based strategy to fabricate 3D nanostructured films composed of rGO decorated with naked Pt-nanocubes (PtNPs) with nanozyme features is proposed and applied to construct affordable lab-made sensors designed to host living cells and assess their cytopathology state (Fig. 1).

3.1. Laser-assembling of the PtNPs-rGO film and morphochemical characterization

The PtNPs-rGO nanostructured film was obtained using a CO_2-laser plotter-induced co-reduction taking advantage of the laser-engraving mode. This procedure is reported in detail in section 2.3 (see Fig. S1) and allows to obtain customized nanostructuring, according to the needed design. In brief, the platinum salt and the GO were co-filtered, and then subjected to CO_2 laser treatment; the film color variation from grey/brown to black visually confirms the successful reduction of GO to rGO and Pt (II) to PtNPs (the presence of platinum nanostructures is demonstrated further in this section). To obtain a uniform film transfer that macroscopically appears uniform without cracks or holes, different rGO precursor (i.e. GO) and platinum precursor amount ratios were tested. The amount of GO to form the film to be transferred (1 mg mL^{-1} x 5 mL) was consistent with Della Pelle et al. (Della Pelle et al., 2023), while the Pt(II) amount to be integrated into the film (30 mM Pt (II)) resulted the same used by Scroccarello et al. (2023). The use of non-optimal amounts of GO and Pt (II) in the production of the film leads to partial film transferring and damage to the nitrocellulose support.

The CO_2-laser-induced morphological and chemical changes were studied via scanning electron microscopy (SEM), x-ray photoelectron spectroscopy (XPS), and Raman spectroscopy; the PtNPs-rGO film was characterized after the transfer onto the NTC substrate since it is the conformation used for sensing. Fig. 2a shows the GO-Pt(II) film before laser treatment, while Fig. 2b, including the inset, depicts the laser-treated film micrographs at low and high magnifications.

Micrographs highlight how the laser treatment induces a significant morphological variation of the film; the Pt(II)-GO film (Fig. 2a) appears smooth and highly packed, whereas the PtNPs-rGO film (Fig. 2b) appears exfoliated and characterized by jagged lamellar nanostructures, with flakes projected out of the plane arranged in a 3D network. Fig. S2a reports the micrograph of NTC/rGO-PtNPs, where the nanostructured film appears continuous, uniform, and without microcracks or holes. The SEM micrograph magnification of the PtNPs-rGO film in Fig. 2b inset, and the elemental mapping of Fig. 2c, highlights the platinum nanostructures formed during the laser treatment; the laser engraving drives the reduction of Pt(II) to Pt(0), forming rectangular/cubic shaped PtNPs homogeneously distributed onto the rGO. The nanocubic nature of the platinum nanostructures, distributed onto the rGO surface, can be better appreciated in Fig. S2b; the PtNPs possess a mean lateral size of 15 ± 6 nm, the size distribution has been calculated sampling 100 nanoparticles using ImageJ, v.1.49.p. It should be noted that the film is conductive only after laser treatment.

The observed micro morphological variations are typical of GO films treated with CO_2-laser since the laser provides photothermal energy in

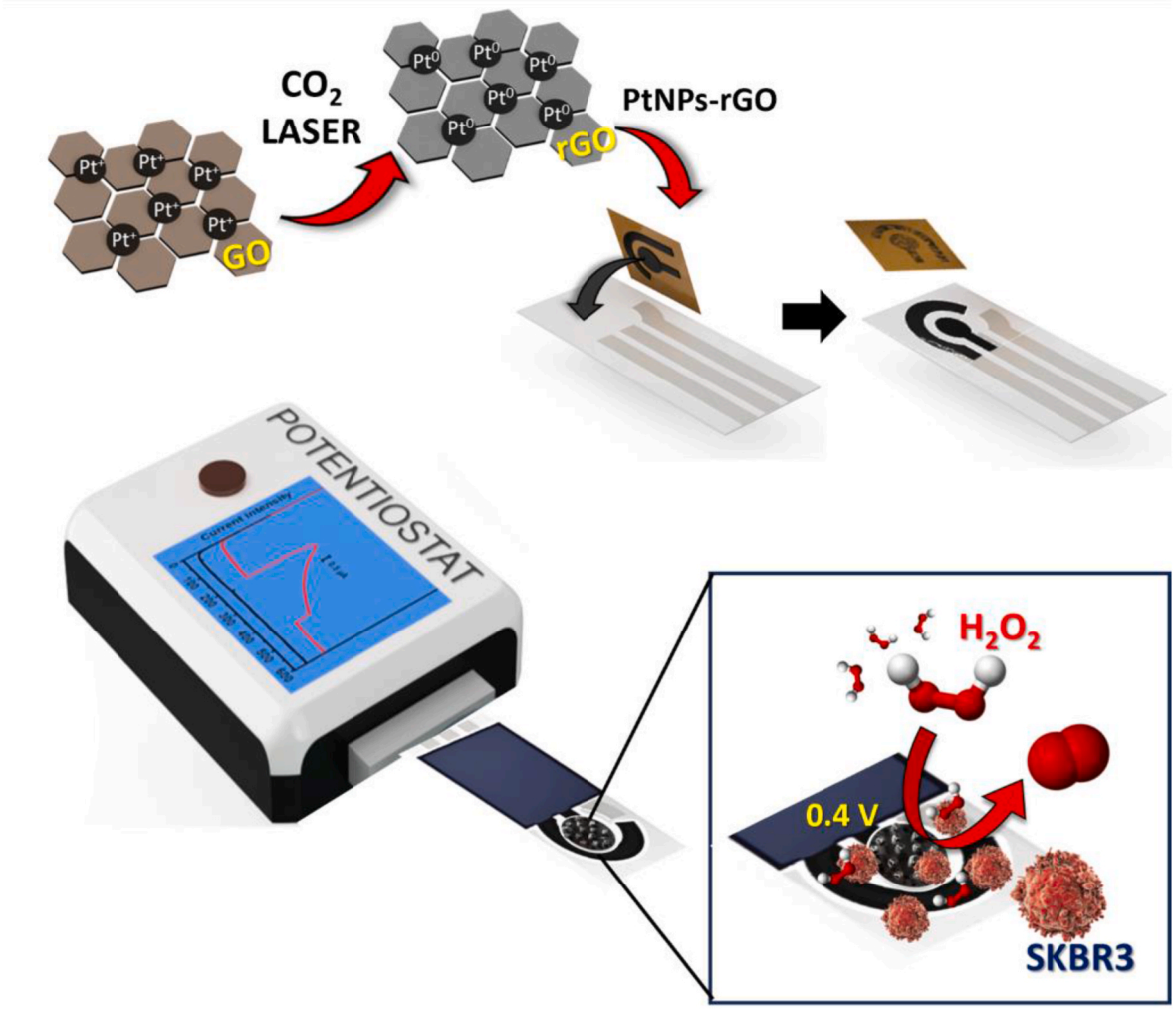


Fig. 1. Graphical sketch of the NTC/PtNPs-rGO sensor components and its use for SKBR3 cell analysis.

the IR region ($\lambda = 10.6$ μm) able to induce a strong oxygen displacement. This phenomenon leads to the removal of hydroxyl (-OH), carboxyl (-COOH), and epoxy (-C-O-C-) groups of the GO (Griffiths et al., 2014; Lei et al., 2020; Rodriguez et al., 2020) with consequent cracking, layers de-stacking, and out-plane expansion of the film, that eventually results in a highly exfoliated 3D rGO framework. On the other hand, the ability of the CO_2 laser to drive the formation of metal nanoparticles on graphenic substrates has been recently demonstrated (Scroccarello et al., 2023).

The rGO-PtNPs formation can be summarized as a CO_2-laser plotter-induced co-reduction process, briefly resumed as follows. The laser instantly increases the GO temperature, inducing atom excitation and expulsion of oxygen groups, forming the conductive rGO film 3D network. At the same time, the high-energy process drives the conversion of the metal source (Pt(II)) to the zero-valent metal state; this process is probably favored by the electron excitation of the graphene caused by the laser-induced photothermal energy. Thus, the platinum ions are reduced and converted in PtNPs anchored onto the rGO network, with a peculiar shape and dimensions energetically favored (Scroccarello et al., 2023).

To shed light on the chemistry of the formed nanostructures Raman and XPS spectroscopy was also carried out. The Pt(II)-GO and PtNPs-rGO films Raman spectra (Fig. 2d), highlight the definition of the G, D, and 2D bands characteristic of exfoliated graphene in the laser-treated film; the untreated film is characterized by G and D peaks with similar intensity characteristic of the GO. In particular, the PtNPs-rGO film is characterized by the appearance of a pronounced and resolved 2D band centered at 2712.0 ± 7.2 cm^{-2}, and a significant decrease of the I_D/I_G band ratio that changes from 0.97 ± 0.02 to 0.44 ± 0.04, for Pt(II)-GO (untreated) to PtNPs-rGO (treated). The D- and G-bands resulted centered at 1353.31 ± 6.3 cm^{-2} and 1577.4 ± 4.8 cm^{-2} for the PtNPs-rGO, and 1348.4 ± 4.3 cm^{-2} and 1591.82 ± 6.7 cm^{-2} for the Pt(II)-GO. These Raman changes are overall attributable to the laser treatment that causes an increase of the sp^2 carbon domains, accompanied by an increase of the exfoliation degree (Dresselhaus et al., 2010; Hao et al., 2010). These data confirmed that the CO_2-laser treatment induces the reduction of the GO to rGO, caused by the oxygen remotion (confirmed by XPS), which also results in the exfoliation of the material (Dresselhaus et al., 2010; Hao et al., 2010). Noteworthy, the concomitant Pt-nanoparticle formation, does not interfere with the GO reduction process.

XPS spectroscopy was used to investigate the chemistry of the films; particular attention was paid to carbon and platinum evolution. Fig. S2c reports the C1s high-resolution spectrum of Pt(II)-GO, while Fig. 2e the film after the laser treatment (i.e., PtNPs-rGO). The GO-containing film (untreated, Fig. S2c) displays the C–C carbon binding energy (BE) at 284.9 eV, accompanied by significant peaks attributable to hydroxyl/epoxy carbon groups (C–O; BE 286.7 eV) and carbonyl groups (C═O; BE 288.6 eV); the latters are characteristic of GO containing structures and denote a high level of carbon oxygenation (Fornasini et al., 2021; Mazzotta et al., 2015; Rodrigues et al., 2019). After the laser treatment (Fig. 2e) the GO reduction is evident since the C1s high-resolution

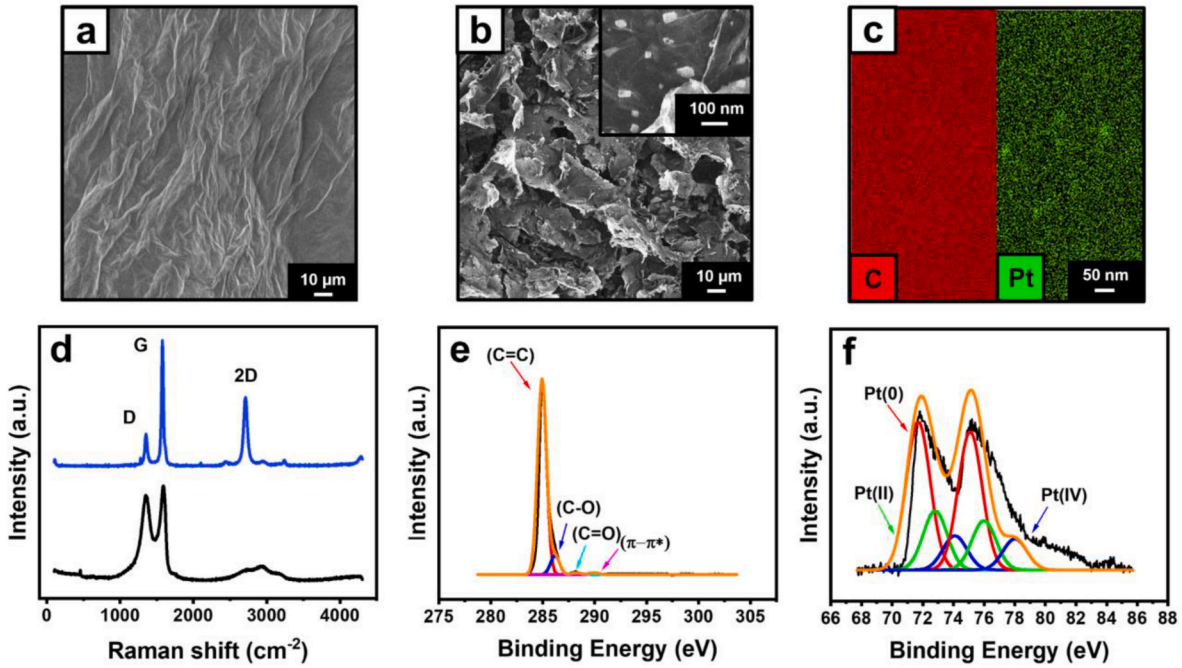


Fig. 2. Morpho-chemical characterization of the NTC/PtNPs-rGO. (**a**) SEM micrograph of GO-Pt (II) film before laser treatment (mag 1.5 K x). (**b**) SEM micrographs (mag 1.5 K x) of PtNPs-rGO after laser treatment; the inset reports a magnification (mag 50 K x) of the same film. (**c**) Elemental mapping of the PtNPs-rGO film, in red the carbon and in green the Pt. (**d**) Raman spectra of the Pt (II)-GO (black line) and PtNPs-rGO (blue line) films. XPS high-resolution spectra of (**e**) C1s and (**f**) Pt4s acquired for the PtNPs-rGO film.

spectrum is characterized by the dominant occurrence of a sharp peak at 284.9 eV due to sp^2-hybridized carbon (C═C), and the almost total disappearance of the C–O and C═O peaks (Fornasini et al., 2021; Mazzotta et al., 2015; Rodrigues et al., 2019). On the other hand, Fig. S2d (untreated film) and Fig. 2f (treated film) report the Pt4f high-resolution spectra, where the variation of the Pt valence state is pointed out. As expected in the Pt (II)-GO film (Fig. S2d), the Pt4f spectrum displays peaks due to Pt (II) (BE 72.1 and 76.0 eV) and Pt (IV) (BE 73.9 eV); interestingly, electron doublets at 70.9 eV and 75.1 eV characteristic of Pt (0) were also observed. The latters can be attributable to the Pt cations' complexation with the GO; this ability of the GO to give complex has been attributed to its intrinsic chemistry (electron doublets, electron vacancies, free electrons, etc.) (Şen and Gökağ;aç, 2007; Smirnov et al., 2016). After the laser treatment (Fig. 2f), the PtNPs-rGO film platinum chemistry is dominated by a sharp electron doublet with BE at 71.7 eV and 75.1 eV, which states the reduction of Pt (II) to Pt(0). The Pt reduction is further confirmed by the spin-orbit splitting that shows a value of 3.4 eV, close to the value of the metallic bulk platinum (Proa-Coronado et al., 2018; Şen and Gökağ;aç, 2007; Smirnov et al., 2016; You et al., 2020); on the other hand, this value is higher for the untreated film (4.2 eV).

3.2. NTC/PtNPs-rGO electrochemistry

The PtNPs-rGO nanostructured film was integrated into a nitrocellulose (NTC) lab-made sensor. The sensor manufacturing procedure is reported in detail in section 2.3(see Fig. S1) and is based on the electronic contacts stencil-printing and the PtNPs-rGO film press transfer. The proposed manufacturing procedure allows multiple fabrications of sensors with the desired design.

To assess the crude electrochemistry of the sensor, cyclic voltammetry (CV) was run in PB for the NTC/PtNPs-rGO sensor; an NTC/rGO sensor (same manufacturing, in absence of platinum) and commercial screen-printed electrode (SPE) were used as control (Fig. 3a).

The NTC/PtNPs-rGO voltammogram profile (blue curve) proves the presence of PtNPs, highlighted by the characteristic oxidation/reduction

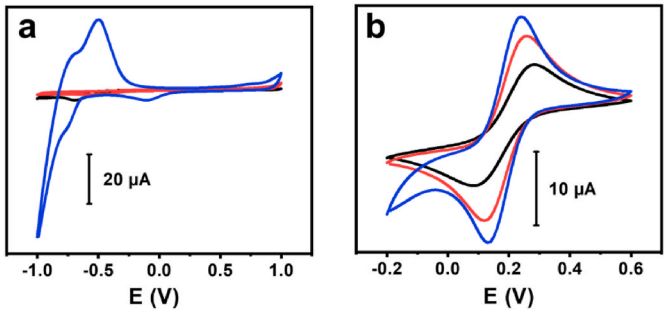


Fig. 3. Electrochemistry of the NTC/PtNPs-rGO. (**a**) Cyclic voltammograms obtained in PB at 20 mV s^{-1} at the SPE (black line), NTC/rGO (red line), and NTC/PtNPs-rGO (blue line). (**b**) Cyclic voltammograms recorded in 1 mM $[Fe(CN)_6]^{3-/4-}$ in 0.1 M KCl at 20 mV s^{-1} at the SPE (black line), NTC/rGO (red line), and NTC/PtNPs-rGO (blue line).

peaks, as well as by the catalytic behavior reported at negative potentials (≤−0.2 V) (Habrioux et al., 2009; Mazzotta et al., 2021; Zhang et al., 2019); this profile has been attributed to the presence of nano-platinum since it is not present in NTC/rGO and SPE, and further confirm the laser-induced formation of platinum nanostructures in the PtNPs-rGO film. The NTC/PtNPs-rGO electrochemistry is described in deep in the next section, where it is studied concerning H_2O_2-induced variation.

The electron transfer ability of the NTC/PtNPs-rGO sensor was investigated using $[Fe(CN)_6]^{3-/4-}$ as redox probe. Fig. 3b displays cyclic voltammograms obtained for the NTC/PtNPs-rGO (blue curve), NTC/rGO (red curve) and SPE (black curve). A quasi-reversible electrochemical behavior was evidenced for both NTC/PtNPs-rGO (ΔE 105 ± 5 mV) and NTC/rGO (ΔE 136 ± 3 mV), with anodic peak currents ($i_{p,a}$) of 19.2 ± 1.3 and 15.0 ± 1.1 μA; the improvement in reversibility is brought by the PtNPs. Significantly lower values were obtained for SPE (ΔE 281 ± 7 mV; $i_{p,a}$ 10.3 ± 0.8 μA). Electrochemical active surface area (ECSA) and heterogeneous electron transfer rate constant (k^0) were also

investigated. The ECSA was extrapolated using the Randles Sevcik theory (Bard and Faulkner, 2002) and the K^0 was calculated using the Nicholson approach (Nicholson, 1965), performing scan rate studies (Silveri et al., 2022). The NTC/PtNPs-rGO ECSA (18.3 ± 1.2 mm^2) and K^0 ($9.7x10^{-3}\pm3.1x10^{-4}$ cm s^{-1}) resulted significantly higher compared to the NTC/rGO (ECSA: 15.7 ± 0.9 mm^2; K^0: $5.6 \times 10^{-3}\pm2.0x10^{-4}$ cm s^{-1}) and SPE (ECSA: 6.3 ± 0.4 mm^2; K^0: $8.0x10^{-4}\pm3.2x10^{-5}$ cm s^{-1}). Overall, the ECSA of the NTC/sensors result improved by the nanostructuration of the film, which after the transfer onto the NTC still retains the 3D dimensionality conferred by the laser; this is possible thanks to the porous structure of the NTC. Furthermore, the homogeneously distributed Pt nanostructures along the PtNPs-rGO film doubled the electron transfer ability of the rGO, and as reported in the next section, confer electrocatalytic features towards H_2O_2.

The NTC/PtNPs-rGO long-term stability was tested using different sensors towards 1 mM $[Fe(CN)_6]^{3-/4-}$ via CVs (Fig. S3), performing measurements every 10 days, storing the sensors at room temperature, in the dark. Evaluating the anodic peak intesity retention, the sensors returned stable responses over 30 days (RSD $\leq$11.3%).

3.3. NTC/PtNPs-rGO electrocatalytic mechanism and electroanalytical performance

The electroanalytical potential of NTC/PtNPs-rGO was challenged for the direct detection of H_2O_2, given the well-known peroxidase-like properties of platinum nanostructures (Mazzotta et al., 2021). Fig. 4a reports the CVs of PB with the addition of increasing amounts of H_2O_2 at the NTC/PtNPs-rGO.

In the absence of H_2O_2, the PtNPs-rGO chemistry is dominated by the voltammetric profile characteristic of polyoriented platinum-containing surfaces (Mazzotta et al., 2021; Zhang et al., 2014), the profile is characterized by an oxidation shoulder at about - 0.7 V, a prominent anodic peak a t - 0.49 V, and a lower peak at 0.76 V; in the reverse scan, a reduction slight peak at −0.10 V and a cathodic shoulder at −0.75 V was observed. The multiple peaks placed at potential $\leq$ −0.2 V can be attributed to the hydrogen adsorption-desorption region, and are attributed to different platinum facets characteristic of the polycrystalline nature of spherical Pt nanostructures. The anodic peak at higher anodic potential and the reverse cathodic peak, close to zero V, are attributable to the platinum oxide formation and reduction, respectively. Overall, the intensity of these characteristic peaks is more

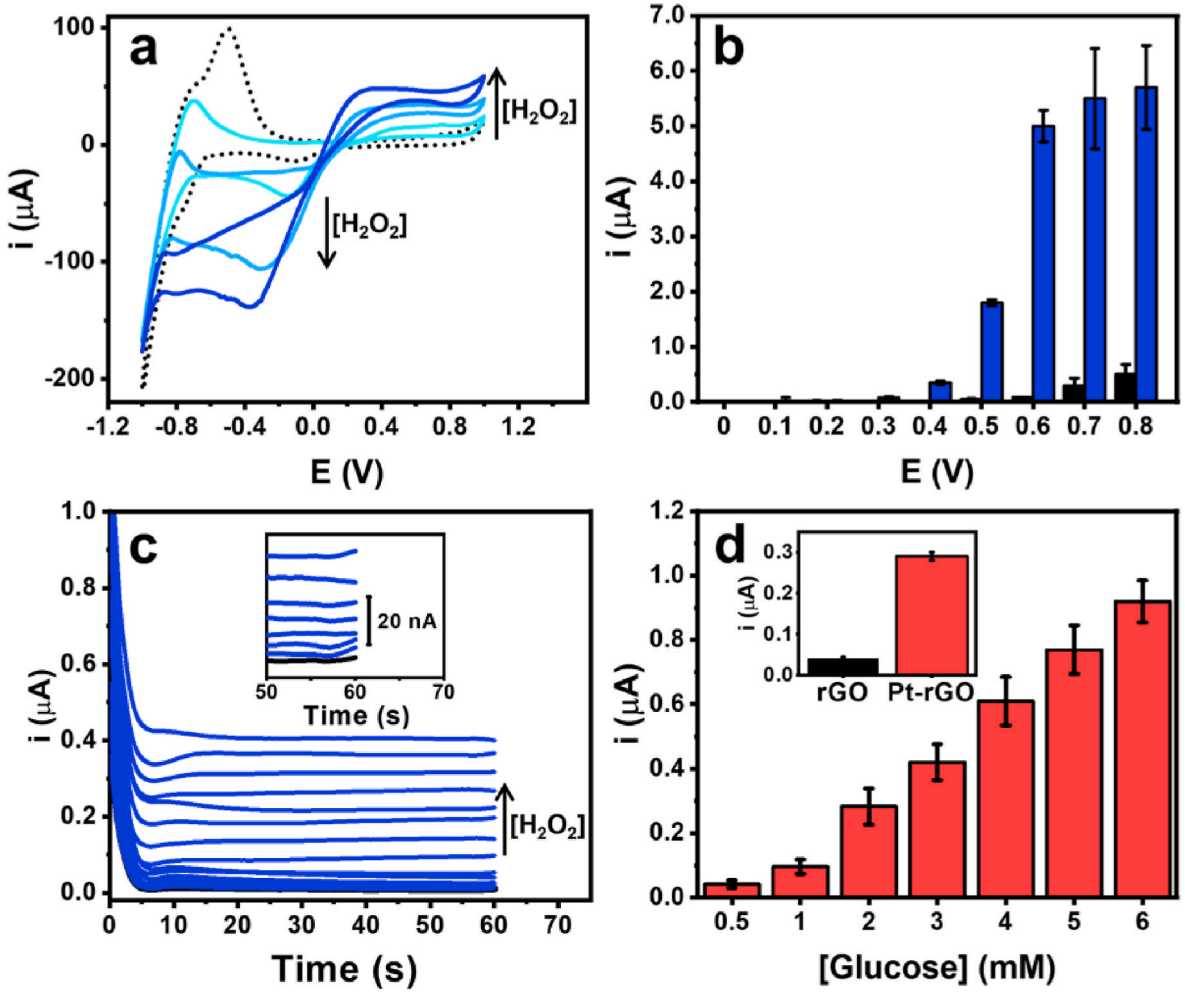


Fig. 4. NTC/PtNPs-rGO nanozyme feature and sensing ability. (**a**) Cyclic voltammograms on NTC/PtNPs-rGO in PB only (dashed black line), and PB with increasing H_2O_2 amounts (i.e., 1, 3, 6 mM); scan rate: 20 mV s^{-1}. (**b**) Amperometric response at different potentials in PB in presence of 50 μM H_2O_2 at the NTC/PtNPs-rGO (blue bar) and NTC/rGO (black bar). (**c**) Chronoamperometry at increasing amounts of H_2O_2 (0.5–80 μM) in PB performed with the NTC/PtNPs-rGO using +0.4 V as working potential; the inset reports a magnification of the final part of amperometry for H_2O_2 at the lower concentrations (0.5–8 μM). (**d**) Current intensities obtained via chronoamperometry at the NTC/PtNPs-rGO modified with glucose oxidase in PB, under increasing concentrations of glucose (0.5–6 mM); working potential +0.4 V. The inset reports the 'delta' of the response of NTC/rGO and NTC/PtNPs-rGO, obtained in the presence and absence of GOx, measuring 2 mM glucose; the delta is intended as the amperometric current recorded at 60 s obtained with sensors modified with 0.25 U of GOx subtracted of the current obtained with the same sensors without GOx.

pronounced for small platinum nanostructures, since the higher surface exposure (Mazzotta et al., 2021). On the other hand, in the CVs recorded in presence of increasing H_2O_2 amounts, a significant and concentration-proportional overall peaks displacement was observed, suggesting that platinum undergoes a change of surface chemistry in the presence of this oxidant. In particular, a cathodic current increase in the negative potential window, and an anodic peak current increase in the positive potential window were recorded; this is typical of an electrocatalytic process where H_2O_2 is reduced through a PtNPs-mediated catalytic process (Guascito et al., 2008). Is well known that this process is driven by the Pt surface sites interacting with hydrogen peroxide, where the measured current is not directly related to the H_2O_2 reaction but is attributed to the PtNPs surface regeneration (Mazzotta et al., 2021). In the laser-assembled NTC/PtNPs-rGO sensor, the nanoplatinum is intercalated/supported in the rGO film, that allows to host the catalytic element in a 3D scaffold and, as demonstrated in section 3.2, to improve the electrochemical active surface area and the heterogeneous electron transfer rate. The catalytic event produced by H_2O_2 induces a PtNPs electronic state rearrangement (Mazzotta et al., 2021), where the 3D rGO film intercepts and effectively shuttles the electrons acting as a nanostructured conductive scaffold.

With the ultimate goal of monitoring H_2O_2 released from live cells integrated into the sensor, chronoamperometry was employed to increase the sensitivity and avoid scanning high overpotentials. To evaluate the contribution of the PtNPs and select the working potential, hydrodynamic voltammetry was performed with the NTC/rGO and NTC/PtNPs-rGO; the anodic potential window was investigated since no reproducible results were obtained in the cathodic region. The hydrodynamic currents reported in Fig. 4b show the responses of the NTC/ sensors at different applied potentials (from 0.0 to +0.8 V), the data incontrovertibly demonstrated the PtNPs role, which reduced the overpotential required and enhanced the response intensity confirming its catalytic role. As a compromise between low overpotential and the signal obtained, +0.4 V was chosen for the following studies.

Fig. 4c reports the amperometric response of the NTC/PtNPs-rGO under consecutive addition of increasing concentration of hydrogen peroxide in PB at +0.4 V; Fig. S4 reports the relative linear dose-response curve obtained. The measurements were carried out simply by placing 30 μL of working solution on the NTC measuring area. The signal obtained is linear from 0.5 to 80 μM ($R^2 = 0.9943$) with a limit of detection (LOD) of 0.2 μM; the LOD was calculated using the formula $LOD = 3\sigma/S$ where σ is the standard deviation of the intercept and S the average (n = 3) slope of the calibration curve. The NTC/PtNPs-rGO returned reproducible results with measurements run with different sensors (RSD ≤13 %, n = 3), as well as evaluating three different calibration curves obtained using three sensors ($NTC/PtNPs\text{-}rGO_{slope}$ RSD ≤5 %, n = 3). The inter-sensor precision endorses the robustness of the PtNPs-rGO film laser-assembling and the sensors' fabrication strategy.

Taking a look at the literature, the LOD, sensitivity, and linear range obtained are improved compared to electrochemical sensors devoted to real-time detection of ROS released by SKBR3 cells. To the best of our knowledge only two papers deals with SKBR-3; this can be attributed to the use of more resistant cell lines, with more standardised behavior and culture protocols. Liu et al. (2014) proposed a carbon-based ink coupled to a paper-based disk decorated with PtNPs via drop-casting. SKBR-3 cells were immobilized onto the paper disk using aptamers, and anticancer drugs were screened by evaluating the H_2O_2 produced by the cells (Liu et al., 2014); in this case, since it is a pioneering communication, the figures of merit were not studied. More recently, Zhang et al. (Liu et al., 2019) proposed a sensor for the detection of superoxide anion released by SKBR-3 cells; a commercial screen-printed electrode was modified via drop-casting cobalt nanoparticle doped porous cubic carbon derived from zeolitic imidazolate framework-67. A sensitivity of 3.6 $\times 10^{-4}$ mA μM^{-1} cm^{-2} and a limit of detection of 0.4 μM were obtained; in this work, the release of ROS was triggered by the injection of the stimulating drug Zymosan A.

PtNPs were mainly used as a modifier for commercial/conventional electrodes, but not to produce transferable conductive films wirh catalytic features; moreover, complete paper-based electrochemical sensors for cell measurements are not reported. PtNP-based sensors preparation still presents limits, commercial electrodes are mainly used, and biological elements are often required; more importantly, dedicated cumbersome synthesis and immobilization procedures are still required for the manufacturing of sensors containing PtNPs. Summing up, the main advancement of the developed sensors relies on the ease and fast production and integration of catalytic components by using lab-grade equipment, maintaining the performances to fulfill the scope.

Before challenging the sensor with live cells, the NTC/PtNPs-rGO ability to host biological elements and detect H_2O_2 was tested; this test aimed to prove the ability of the sensors, to detect H_2O_2 released by biological elements adhered on the sensing nanostructured scaffold. To this aim, glucose oxidase (GOx) from Aspergillus niger (Type X–S lyophilized powder; 50 KU g^{-1}), was employed and the H_2O_2 produced by the glucose conversion targeted; different amounts of glucose were employed to simulate different external stimuli toward the biological element. The GOx amount and the measuring time were firstly optimized (Figs. S5a–b), and later the dose-response curve was evaluated under increasing amounts of glucose. The NTC/PtNPs-rGO was straightforwardly obtained by absorption of 0.25 U of GOx onto the NTC sensor measuring zone (left dry in the dark); measurements were performed leaving the biosensor to react with the substrate for 15 min. In Fig. 4d the current response intensities obtained are shown and the relative linear fit is reported in Fig. S5c. The NTC/PtNPs-rGO was able to host GOx returning linear responses ($R^2 = 0.9964$; RSD ≤12 %, n = 3) for glucose concentration in the 0.5–6 mM range, demonstrating the sensor's ability to host bio-catalytic events. Fig. 4d inset reports the response for NTC/rGO and NTC/PtNPs-rGO, obtained in the presence and absence of GOx, for 2 mM glucose. The NTC/PtNPs-rGO returns a signal close to phosphate buffer (PB) only, proving that the response is due to the H_2O_2 produced by the GOx activity; on the other hand, the NRT/rGO response is 14-fold lower, further proving the active role of the nPt for the H_2O_2 signal amplification.

3.4. NTC/PtNPs-rGO integrating cells. Real-time detection of H_2O_2 release under PMA stimulation

Tests performed with sensors in presence of cells were conducted according to section 2.5; in brief, the sensor was incubated in the cell culturing medium (24 h) to adhere the cells to the sensing surface, then, the culturing medium was removed, and amperometric measurements were run in PB.

The first step was to demonstrate that the NTC/PtNPs-rGO sensor was not cytotoxic for SKBR3 and Vero cells a tumorigenic and a non-tumorigenic cell line, respectively (see section 2.5); this test was also conducted to evaluate the adhesion capacity of the cells on the sensing surface. The cells were seeded in modified 35 mm plates containing the NTC/PtNPs-rGO sensor. After 24 h of incubation, cell viability was evaluated using the Live/Dead viability/Cytotoxicity kit; experiments were performed in triplicate. As shown in the micrograph of Fig. 5a (SKBR3, $1x10^5$ cells), the cells were viable (green fluorescence due to esterase activity) and adhered to the PtNPs-rGO surface, proving the cytocompatibility of the sensing material and the ability of the cells to stay in direct contact with the sensor.

Before the cell stimulation study, the measuring set-up was tested using H_2O_2 to simulate the stimulation effect. The NTC/PtNPs-rGO sensor was incubated in the cell culturing medium, afterward, the culturing medium was removed, and amperometry was run in PB. After the signal stabilization, different H_2O_2 amounts were added. Linear ($R^2 = 0.9935$) and reproducible (RSD ≤14 %, n = 3) responses between 10 and 300 μM were obtained (Fig. S6a), endorsing the sensor's working ability in presence of cells. Comparing the calibration curves obtained in absence (Fig. S4; y = 0.00508x+0.01012) and in presence (Fig. S6, y =

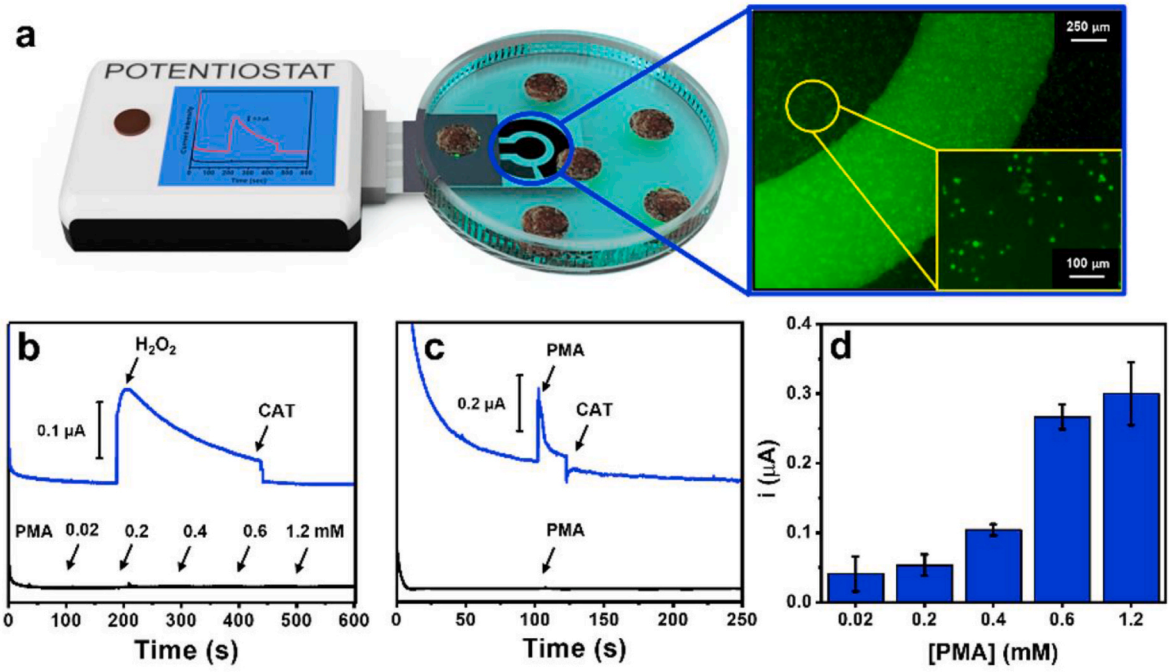


Fig. 5. NTC/PtNPs-rGO integrating SKBR3, sensing ability. (**a**) Graphical sketch of the NTC/nP-rGO sensor during cell culture. The zoom reports the micrographs of the viable SKBR3 cancer cells, highlighted by green fluorescence, after 24 h of culturing in presence of the NTC/PtNPs-rGO (immediately before PMA-stimulation). (**b**)Blue curve: Amperometric response of 30 μM H_2O_2 in the NTC/PtNPs-rGO sensor in presence of SKBR3 cells, and signal suppression induced by catalase (CAT). Black curve: chronoamperometry signal under the addition of increasing amounts of PMA on the NTC/PtNPs-rGO without cells. (**c**) Blue curve: amperometric response of NTC/PtNPs-rGO integrating SKBR3 cells under the addition of 0.6 mM PMA, and signal suppression induced by catalase (CAT); Black curve: amperometric response of NTC/PtNPs-rGO integrating Vero cells under the addition of 0.6 mM PMA. (**d**) Amperometric currents obtained at the NTC/PtNPs-rGO integrating SKBR3 cells, under the addition of increasing concentrations of PMA. All the amperometric measurements were performed at +0.4 V in phosphate buffer.

0.0026x-0.003) of cells, the lower sensitivity, in the latter case, can be attributed to the limited diffusion of the H_2O_2; this observation, together to Fig. 5a micrograph, confirm the cells adhesion on the nanostructured sensing surface. The presence of cells influences also the linear range that is narrower. A typical amperometric signal obtained is reported in Fig. 5b (blue curve), where the attribution of the peak response to H_2O_2 was confirmed by the addition of 10 μL catalase (50 U mL^{-1}), which caused a sudden drop of current. The catalase test is typically used in sensors devoted to measuring ROS released by cells, to confirm that the recorded signal is caused by H_2O_2, given the enzyme's ability to decompose the hydrogen peroxide into water and oxygen bringing an immediate decay of current (Rojas et al., 2018, 2020). Additionally, the ability of the PMA to react in a not specific manner, i.e. in absence of the cells, has been also checked; Fig. 5b (black curve) reports the response of NTC/PtNPs-rGO (without cells), under additions of increasing concentrations of phorbol 12-myristate 13-acetate (PMA, from 0.02 to 1.2 mM); no peaks were recorded.

The H_2O_2 release from cells stressed with PMA was then assessed. Two different cell lines were selected a non-tumorigenic (Vero cells) and a tumorigenic (SKBR3 cells). PMA has been demonstrated to induce ROS production in different cell lines (Jin et al., 2021). ROS are secondary messenger signaling; in healthy cells, the ROS level is low because there is a balance between oxidants and antioxidants. Cancer cells tend to produce higher amounts of H_2O_2, impairing the redox balance. This affects proliferation, migration, invasion, and angiogenesis rates, which in turn favors the growth of the tumor. Excess cellular levels of ROS can also induce apoptosis (Nakamura and Takada, 2021). A typical measurement on the NTC/PtNPs-rGO sensor integrating SKBR3 cells under PMA stimulation is shown in Fig. 5c (blue curve); the response of the sensor to PMA is evident and confirmed by the suppression of the signal caused by the addition of catalase. On the other hand, in Fig. 5c (black line) the NTC/PtNPs-rGO sensor integrating Vero cells (non-tumorigenic), did not return any signal under the addition of PMA; this, in accordance with the literature, indicates no detectable H_2O_2 production (Chang et al., 2020; Rojas et al., 2022). The dependence of the current recorded on different loads of SKBR3 cells ($0.5x10^5$, $1x10^5$ and $2x10^5$ cells) was also studied (Fig. S6b). An increase in the current was observed with the increase in the cell density; $1x10^5$ was confirmed to be the best compromise between the signal obtained and measurement reproducibility (RSD = 7 %, n = 3). Fig. 5d indicates that under the addition of different concentrations of PMA, from 0.02 mM to 0.6 mM, increasing signals are obtained; beyond 0.6 mM PMA no incresing analytical responses were observed, this behavior may be attributed to a saturation of the stimulus for the cells. Estimation of the signals using the dose-response curve in the presence of SKBR3 cells in the same measuring configuration (Fig. S6a), gave H_2O_2 levels between 17 μM and 104 μM; it should be mentioned that this quantification is a rough estimation of the H_2O_2 released, since, the analyte is released by the cells, and not added as for the dose-response experiments.

Overall, the obtained results prove that the NTC/PtNPs-rGO sensors can host viable cells, allowing the monitoring of their physiological state through the on-site and real-time evaluation of the H_2O_2 release under chemical stimulation. Moreover, the sensors give quantitative information on the released H_2O_2, allowing correlation of concentration with the cellular activity and, therefore, the progression of the pathological process.

4. Conclusions

A highly exfoliated 3D film based on reduced graphene oxide integrating naked platinum nanocubes, which possesses nanozymatic features, was straightforwardly assembled using a CO_2 laser plotter; the formation of the nanodecorated sensing film relies on the instantaneous and simultaneous reduction of graphene oxide and platinum cations to a conductive nanostructured rGO/zero-valent PtNPs transferable film. The PtNPs-rGO film was successfully integrated into NTC substrate

giving rise to fully lab-made sensors that were produced via a semi-automated approach based on benchtop instrumentation and office substrates. The laser-assembled sensing 3D conductive PtNPs-rGO network proved an electrocatalytic activity that allowed direct and bio-mediated sensitive and reproducible detection of H_2O_2. The NTC/PtNPs-rGO sensor is able to host live cells and was tested for the monitoring of H_2O_2 released from non-tumorigenic and tumorigenic cell lines stimulated with phorbol-12-myristate-13-acetate. The NTC/PtNPs-rGO proved to be able to return on-site and real-time quantitative information of the H_2O_2 released by the stimulated hosted cells and to follow-up cell activity. The promising results obtained with the proposed technology pave the way for the monitoring of the cytopathology state of cancer cells via the screening of their oxidative stress/redox homeostasis trought the use of easy-to-use everyone-reach point-of-care devices.

CRediT authorship contribution statement

Qurat U.A. Bukhari: Writing – original draft, Visualization, Validation, Methodology, Investigation. **Flavio Della Pelle:** Writing – review & editing, Writing – original draft, Visualization, Validation, Project administration, Investigation, Data curation, Conceptualization. **Ruslan Alvarez-Diduk:** Writing – review & editing, Visualization, Validation, Supervision, Project administration, Methodology, Investigation, Conceptualization. **Annalisa Scroccarello:** Writing – original draft, Visualization, Validation, Methodology, Formal analysis, Data curation. **Carme Nogués:** Writing – review & editing, Validation, Supervision, Methodology, Investigation, Conceptualization. **Oriol Careta:** Writing – review & editing, Visualization, Validation, Methodology, Investigation. **Dario Compagnone:** Writing – review & editing, Supervision, Resources, Funding acquisition. **Arben Merkoci:** Writing – review & editing, Supervision, Resources, Funding acquisition.

Declaration of competing interest

The authors declare that they have no known competing financial interests or personal relationships that could have appeared to influence the work reported in this paper.

Data availability

No data was used for the research described in the article.

Acknowledgments

This work has received funding from the European Union's Horizon 2020 research and innovation programme under the Graphene Flagship grant agreement no. 881603. The support received is also acknowledged by R. Alvarez. Views and opinions expressed are however those of the authors only and do not necessarily reflect those of the European Union. The European Union cannot be held responsible for them. The ICN2is funded by the CERCA programme/Generalitat de Catalunya. The ICN2 is supported by the Severo Ochoa Centres of Excellence programme, Grant CEX2021-001214-S, funded by MCIN/AEI/10.13039.501100011033. This research was funded by the European Union – Next Generation EU. Project Code: ECS00000041; Project CUP: C43C22000380007; Project Title: Innovation, digitalization and sustainability for the diffused economy in Central Italy – VITALITY. F.D.P. and D.C. acknowledge the Ministry of Education, University and Research (MIUR) and European Social Fund (ESF) for the PON R&I 2014–2020 program, action 1.2′AIM: Attraction and International Mobility' (AIM1894039-3). We acknowledge Departament de Recerca i Universitats of Generalitat de Catalunya for the grant 2021 SGR 01464 and 2021 SGR 00122 and Grant PID2021-124795NB-I00 and PID2020-116844RB-C21 funded by MCIN/AEI/10.13039/501100011033 and by "ERDF A way of making Europe".

Appendix A. Supplementary data

Supplementary data to this article can be found online at https://doi.org/10.1016/j.bios.2024.116544.

References

Bard, A.J., Faulkner, L.R., 2002. Electrochemical methods: fundamentals and applications. Russ. J. Electrochem. 38, 1364–1365. https://doi.org/10.1023/A:1021637209564.

Chang, S.N., Dey, D.K., Oh, S.T., Kong, W.H., Cho, K.H., Al-Olayan, E.M., Hwang, B.S., Kang, S.C., Park, J.G., 2020. Phorbol 12-myristate 13-acetate induced toxicity study and the role of tangeretin in abrogating hif-1α-nf-κb crosstalk in vitro and in vivo. Int. J. Mol. Sci. 21, 1–22. https://doi.org/10.3390/ijms21239261.

Coroş, M., Pruneanu, S., Stefan-van Staden, R.-I., 2020. Review—recent progress in the graphene-based electrochemical sensors and biosensors. J. Electrochem. Soc. 167, 037528 https://doi.org/10.1149/2.0282003jes.

Della Pelle, F., Bukhari, Q.U.A., Álvarez-Diduk, R., Scroccarello, A., Compagnone, D., Merkoçi, A., 2023. Freestanding laser-induced two dimensional heterostructures for self-contained paper-based sensors. Nanoscale 15, 7164–7175. https://doi.org/10.1039/d2nr07157f.

Dideikin, A.T., Vul, A.Y., 2019. Graphene oxide and derivatives: the place in graphene family. Front. Phys. 6 https://doi.org/10.3389/fphy.2018.00149.

Dong, W., Ren, Y., Bai, Z., Yang, Y., Wang, Z., Zhang, C., Chen, Q., 2018. Trimetallic AuPtPd nanocomposites platform on graphene: applied to electrochemical detection and breast cancer diagnosis. Talanta 189, 79–85. https://doi.org/10.1016/j.talanta.2018.06.067.

Dresselhaus, M.S., Jorio, A., Hofmann, M., Dresselhaus, G., Saito, R., 2010. Perspectives on carbon nanotubes and graphene Raman spectroscopy. Nano Lett. 10, 751–758. https://doi.org/10.1021/nl904286r.

Fornasini, L., Scaravonati, S., Magnani, G., Morenghi, A., Sidoli, M., Bersani, D., Bertoni, G., Aversa, L., Verucchi, R., Riccò, M., Lottici, P.P., Pontiroli, D., 2021. In situ decoration of laser-scribed graphene with TiO2 nanoparticles for scalable high-performance micro-supercapacitors. Carbon N. Y. 176, 296–306. https://doi.org/10.1016/j.carbon.2021.01.129.

Giacomelli, C., Álvarez-Diduk, R., Testolin, A., Merkoçi, A., 2020. Selective stamping of laser scribed rGO nanofilms: from sensing to multiple applications. 2D Mater. 7, 12. https://doi.org/10.1088/2053-1583/ab68a7.

Griffiths, K., Dale, C., Hedley, J., Kowal, M.D., Kaner, R.B., Keegan, N., 2014. Laser-scribed graphene presents an opportunity to print a new generation of disposable electrochemical sensors. Nanoscale 6, 13613–13622. https://doi.org/10.1039/c4nr04221b.

Guascito, M.R., Filippo, E., Malitesta, C., Manno, D., Serra, A., Turco, A., 2008. A new amperometric nanostructured sensor for the analytical determination of hydrogen peroxide. Biosens. Bioelectron. 24, 1057–1063. https://doi.org/10.1016/j.bios.2008.07.048.

Gurunathan, S., Jeyaraj, M., Kang, M.H., Kim, J.H., 2019. Graphene oxide-platinum nanoparticle nanocomposites: a suitable biocompatible therapeutic agent for prostate cancer. Polymers 11. https://doi.org/10.3390/polym11040733.

Habrioux, A., Vogel, W., Guinel, M., Guetaz, L., Servat, K., Kokoh, B., Alonso-Vante, N., 2009. Structural and electrochemical studies of Au-Pt nanoalloys. Phys. Chem. Chem. Phys. 11, 3573–3579. https://doi.org/10.1039/b820668f.

Hao, Y., Wang, Y., Wang, L., Ni, Z., Wang, Z., Wang, R., Koo, C.K., Shen, Z., Thong, J.T.L., 2010. Probing layer number and stacking order of few-layer graphene by Raman Spectroscopy. Small 6, 195–200. https://doi.org/10.1002/smll.200901173.

Inagaki, M., Kang, F., 2014. Graphene derivatives: graphane, fluorographene, graphene oxide, graphyne and graphdiyne. J. Mater. Chem. A 2, 13193–13206. https://doi.org/10.1039/c4ta01183j.

Jiao, J., Pan, M., Liu, X., Li, B., Liu, J., Chen, Q., 2020. A non-enzymatic sensor based on trimetallic nanoalloy with poly (diallyldimethylammonium chloride)-capped reduced graphene oxide for dynamic monitoring hydrogen peroxide production by cancerous cells. Sensors 20, 10.3390/s20010071.

Jin, Y., Dixon, B., Jones, L., Gorbet, M., 2021. The differential reactive oxygen species production of tear neutrophils in response to various stimuli in vitro. Int. J. Mol. Sci. 22 https://doi.org/10.3390/ijms222312899.

Lee, S., Lee, Y.J., Kim, J.H., Lee, G.J., 2020. Electrochemical detection of H2O2 released from prostate cancer cells using Pt nanoparticle-decorated rGO-CNT nanocomposite-modified screen-printed carbon electrodes. Chemosensors 8. https://doi.org/10.3390/CHEMOSENSORS8030063.

Lei, Y., Alshareef, A.H., Zhao, W., Inal, S., 2020. Laser-scribed graphene electrodes derived from lignin for biochemical sensing. ACS Appl. Nano Mater. 3, 1166–1174. https://doi.org/10.1021/acsanm.9b01795.

Lennicke, C., Rahn, J., Lichtenfels, R., Wessjohann, L.A., Seliger, B., 2015. Hydrogen peroxide - production, fate and role in redox signaling of tumor cells. Cell Commun. Signal. 13, 1–19. https://doi.org/10.1186/s12964-015-0118-6.

Li, G., 2020. Direct laser writing of graphene electrodes. J. Appl. Phys. 127 https://doi.org/10.1063/1.5120056.

Liu, F., Ge, S., Yu, J., Yan, M., Song, X., 2014. Electrochemical device based on a Pt nanosphere-paper working electrode for in situ and real-time determination of the flux of H2O2 releasing from SK-BR-3 cancer cells. Chem. Commun. 50, 10315–10318. https://doi.org/10.1039/c4cc04199b.

Liu, M.M., Liu, H., Li, S.H., Zhong, Y., Chen, Y., Guo, Z.Z., Chen, W., Lin, X.H., Lei, Y., Liu, A.L., 2021a. Integrated paper-based 3D platform for long-term cell culture and

in situ cell viability monitoring of Alzheimer's disease cell model. Talanta 223. https://doi.org/10.1016/j.talanta.2020.121738.
Liu, M.M., Liu, H., Li, S.H., Zhong, Y., Chen, Y., Guo, Z.Z., Chen, W., Lin, X.H., Lei, Y., Liu, A.L., Zhang, H., Cai, X., Zhao, H., Sun, W., Wang, Z., Lan, M., 2019. Enzyme-free electrochemical sensor based on ZIF-67 for the detection of superoxide anion radical released from SK-BR-3 cells. J. Electroanal. Chem. 855, 113653 https://doi.org/10.1016/j.jelechem.2019.113653.
Liu, X., Zhang, X., Zheng, J., 2021b. One-pot fabrication of AuNPs-Prussian blue-Graphene oxide hybrid nanomaterials for non-enzymatic hydrogen peroxide electrochemical detection. Microchem. J. 160, 105595 https://doi.org/10.1016/j.microc.2020.105595.
Mazzotta, E., Di Giulio, T., Mastronardi, V., Pompa, P.P., Moglianetti, M., Malitesta, C., 2021. Bare platinum nanoparticles deposited on glassy carbon electrodes for electrocatalytic detection of hydrogen peroxide. ACS Appl. Nano Mater. 4, 7650–7662. https://doi.org/10.1021/acsanm.1c00754.
Mazzotta, E., Rella, S., Turco, A., Malitesta, C., 2015. XPS in development of chemical sensors. RSC Adv. 5, 83164–83186. https://doi.org/10.1039/c5ra14139g.
Meier, J., Ho, E.M., Stapleton, J.A., Iverson, N.M., 2019. Hydrogen peroxide sensors for biomedical applications. Chemosensors 7, 10.3390/chemosensors7040064.
Morais, A., Rijo, P., Batanero, B., Nicolai, M., 2022. Low platinum-content electrocatalysts for highly sensitive detection of endogenously released H2O2. Biosensors 12, 1–23. https://doi.org/10.3390/bios12090672.
Nakamura, H., Takada, K., 2021. Reactive oxygen species in cancer: current findings and future directions. Cancer Sci. 112, 3945–3952. https://doi.org/10.1111/cas.15068.
Nicholson, R.S., 1965. Theory and application of cyclic voltammetryfm measurement of electrode reaction kinetics. Anal. Chem. 37, 1351–1355. https://doi.org/10.1021/ac60230a016.
Proa-Coronado, S., Vargas-García, J.R., Manzo-Robledo, A., Mendoza-Acevedo, S., Villagómez, C.J., Mercado-Zúñiga, C., Muñoz-Aguirre, N., Villa-Vargas, L.A., Martinez-Rivas, A., 2018. Platinum nanoparticles homogenously decorating multilayered reduced graphene oxide for electrical nanobiosensor applications. Thin Solid Films 658, 54–60. https://doi.org/10.1016/j.tsf.2018.05.032.
Rocha, D.P., Ataide, V.N., de Siervo, A., Gonçalves, J.M., Muñoz, R.A.A., Paixão, T.R.L. C., Angnes, L., 2021. Reagentless and sub-minute laser-scribing treatment to produce enhanced disposable electrochemical sensors via additive manufacture. Chem. Eng. J. 130594 https://doi.org/10.1016/j.cej.2021.130594.
Rodrigues, J., Zanoni, J., Gaspar, G., Fernandes, A.J.S., Carvalho, A.F., Santos, N.F., Monteiro, T., Costa, F.M., 2019. ZnO decorated laser-induced graphene produced by direct laser scribing. Nanoscale Adv. 1, 3252–3268. https://doi.org/10.1039/c8na00391b.
Rodriguez, R.D., Khalelov, A., Postnikov, P.S., Lipovka, A., Dorozhko, E., Amin, I., Murastov, G.V., Chen, J.J., Sheng, W., Trusova, M.E., Chehimi, M.M., Sheremet, E., 2020. Beyond graphene oxide: laser engineering functionalized graphene for flexible electronics. Mater. Horiz. 7, 1030–1041. https://doi.org/10.1039/c9mh01950b.
Rojas, D., Della Pelle, F., Del Carlo, M., d'Angelo, M., Dominguez-Benot, R., Cimini, A., Escarpa, A., Compagnone, D., 2018. Electrodeposited Prussian Blue on carbon black modified disposable electrodes for direct enzyme-free H2O2 sensing in a Parkinson's disease in vitro model. Sensor. Actuator. B Chem. 275, 402–408. https://doi.org/10.1016/j.snb.2018.08.040.
Rojas, D., Hernández-Rodríguez, J.F.J.F., Della Pelle, F., Del Carlo, M., Compagnone, D., Escarpa, A., 2020. Oxidative stress on-chip: prussian blue-based electrode array for in situ detection of H2O2 from cell populations. Biosens. Bioelectron. 170, 112669 https://doi.org/10.1016/j.bios.2020.112669.
Rojas, D., Hernández-Rodríguez, J.F.J.F., Della Pelle, F., Escarpa, A., Compagnone, D., 2022. New trends in enzyme-free electrochemical sensing of ROS/RNS. Application to live cell analysis. Mikrochim. Acta 189, 102. https://doi.org/10.1007/s00604-022-05185-w.
Schumacker, P.T., 2015. Reactive oxygen species in cancer: a dance with the devil. Cancer Cell 27, 156–157. https://doi.org/10.1016/j.ccell.2015.01.007.
Scroccarello, A., Ruslan, A., Pelle, F. Della, Carvalho, C. De, Idili, A., Parolo, C., Compagnone, D., Merkoc, A., 2023. One-step laser nanostructuration of reduced graphene oxide films embedding metal nanoparticles for sensing applications. ACS Sens. 8, 598–609. https://doi.org/10.1021/acssensors.2c01782.
Şen, F., Gökağaç, G., 2007. Different sized platinum nanoparticles supported on carbon: an XPS study on these methanol oxidation catalysts. J. Phys. Chem. C 111, 5715–5720. https://doi.org/10.1021/jp068381b.
Silveri, F., Pelle, F. Della, Scroccarello, A., Mazzotta, E., Giulio, T. Di, Malitesta, C., Compagnone, D., 2022. Carbon black functionalized with naturally occurring compounds in water phase for electrochemical sensing of antioxidant compounds. Antioxidants 11, 2008.
Smirnov, M.Y., Kalinkin, A.V., Vovk, E.I., Bukhtiyarov, V.I., 2016. Analysis of the oxidation state of platinum particles in supported catalysts by double differentiation of XPS lines. J. Struct. Chem. 57, 1127–1133. https://doi.org/10.1134/S002247661606010X.
Trujillo, R.M., Barraza, D.E., Zamora, M.L., Cattani-Scholz, A., Madrid, R.E., 2021. Nanostructures in hydrogen peroxide sensing. Sensors 21, 1–26. https://doi.org/10.3390/s21062204.
You, Z., Qiu, Q., Chen, H., Feng, Y., Wang, X., Wang, Y., Ying, Y., 2020. Laser-induced noble metal nanoparticle-graphene composites enabled flexible biosensor for pathogen detection. Biosens. Bioelectron. 150, 111896 https://doi.org/10.1016/j.bios.2019.111896.
Young, A.B., 2009. Four decades of neurodegenerative disease research: how far we have come. J. Neurosci. 29, 12722–12728. https://doi.org/10.1523/JNEUROSCI.3767-09.2009.
Zhang, M., Lv, J.J., Li, F.F., Bao, N., Wang, A.J., Feng, J.J., Zhou, D.L., 2014. Urea assisted electrochemical synthesis of flower-like platinum arrays with high electrocatalytic activity. Electrochim. Acta 123, 227–232. https://doi.org/10.1016/j.electacta.2014.01.054.
Zhang, Y., Zhu, H., Sun, P., Sun, C.K., Huang, H., Guan, S., Liu, H., Zhang, H., Zhang, C., Qin, K.R., 2019. Laser-induced graphene-based non-enzymatic sensor for detection of hydrogen peroxide. Electroanalysis 31, 1334–1341. https://doi.org/10.1002/elan.201900043.
Zhao, L., Rosati, G., Piper, A., Carvalho, C. De, Hu, L., Yang, Q., Della Pelle, F., Alvarez-Diduk, R., Merkoci, A., 2023. Laser reduced graphene oxide electrode for pathogenic Escherichia coli detection. ACS Appl. Mater. Interfaces 15, 9024–9033. https://doi.org/10.1021/acsami.2c20859.
Zhao, S., Zang, G., Zhang, Y., Liu, H., Wang, N., Cai, S., Durkan, C., Xie, G., Wang, G., 2021. Recent advances of electrochemical sensors for detecting and monitoring ROS/RNS. Biosens. Bioelectron. 179, 113052 https://doi.org/10.1016/j.bios.2021.113052.
Zhu, L., Gao, Y.Y., Han, B., Liu, S., Fu, X.Y., Ding, H., Zhang, Y.L., 2019. Programmable laser patterning of Ag nanoparticles and reduced graphene oxide hybrid electrodes for nonenzymatic hydrogen peroxide detection. ACS Appl. Nano Mater. 2, 7989–7996. https://doi.org/10.1021/acsanm.9b02032.